


Synergistic Theranostics of Magnetic Resonance Imaging and Photothermal Therapy of Breast Cancer Based on the Janus Nanostructures $\text{Fe}_3\text{O}_4\text{-Au}_{\text{shell}}$ -PEG

Xun Kang
Tao Sun
Liang Zhang 
Chunyu Zhou
Zhongsheng Xu
Mengmeng Du
Shilin Xiao
Yun Liu
Mingfu Gong 
Dong Zhang

Department of Radiology, Xinqiao
Hospital, Army Medical University,
Chongqing, People's Republic of China

Background: Satisfactory prognosis of breast cancer (BC) is limited by difficulty in early diagnosis and insufficient treatment. The combination of molecular imaging and photothermal therapy (PTT) may provide a solution.

Methods: $\text{Fe}_3\text{O}_4\text{-Au}_{\text{shell}}$ nanoparticles (NPs) were prepared by thermal decomposition, seeded growth and galvanic replacement and were comprehensively characterized. After conjugated to PEG, NPs were used as MRI and PTT agents in vitro and in vivo.

Results: $\text{Fe}_3\text{O}_4\text{-Au}_{\text{shell}}$ NPs which had uniform Janus-like morphology were successfully synthesized. The Fe_3O_4 had a size of 18 ± 2.2 nm, and the Au_{shell} had an outer diameter of 25 ± 3.3 nm and an inner diameter of 20 ± 2.9 nm. The NPs showed superparamagnetism, a saturation magnetization of 36 emu/g, and an optical absorption plateau from 700 to 808 nm. The $\text{Fe}_3\text{O}_4\text{-Au}_{\text{shell}}$ NPs were determined to possess good biocompatibility. After PEG coating, the zeta potential of NPs was changed from -23.75 ± 1.37 mV to -13.93 ± 0.55 mV, and the FTIR showed the characteristic C–O stretching vibration at 1113 cm^{-1} . The NPs' MR imaging implied that the T_2 can be shortened by $\text{Fe}_3\text{O}_4\text{-Au}_{\text{shell}}$ NPs in a concentration-dependent manner, and the $\text{Fe}_3\text{O}_4\text{-Au}_{\text{shell}}$ NPs coated with PEG at the molar ratio of 160 (PEG: NPs) showed the highest transverse relaxivity (r_2) of $216\text{ mM}^{-1}\text{s}^{-1}$. After irradiation at 0.65 W/cm^2 for 5 min, all cells incubated with the $\text{Fe}_3\text{O}_4\text{-Au}_{\text{shell}}$ -PEG160 NPs (Fe: 30 ppm, Au: 70 ppm) died. After administrated intratumorally, $\text{Fe}_3\text{O}_4\text{-Au}_{\text{shell}}$ -PEG160 notably decreased the signal intensity of tumor in T_2 WI images. Under the same irradiation, the temperature of tumors injected with $\text{Fe}_3\text{O}_4\text{-Au}_{\text{shell}}$ -PEG160 quickly rose to 54.6°C , and the tumors shrank rapidly and were ablated in 6 days.

Conclusion: $\text{Fe}_3\text{O}_4\text{-Au}_{\text{shell}}$ -PEG NPs show good r_2 and PTT performance and are promising synergistic theranostic agents of MRI and PTT for BC.

Keywords: magnetic resonance imaging, photothermal therapy, nanoparticle, early breast cancer theranostics, gold nanoshells

Correspondence: Mingfu Gong; Dong Zhang
Department of Radiology, Xinqiao
Hospital, Army Medical University,
No. 183, Xinqiao Street, Shapingba
District, Chongqing, People's Republic of
China
Tel +86 2368763843
Fax +86 2368755306
Email hummer198625@163.com;
hszhang@163.com

Introduction

Breast cancer (BC) has the highest morbidity and mortality among women worldwide.^{1–3} The difficulty of early diagnosis and insufficient treatment are believed to be the two most important factors leading to this situation.⁴ In clinical practice, BC is usually diagnosed by an imaging examination.^{4,5} Imaging screening is critical for the diagnosis and staging of BC and includes mammography, ultrasound, and magnetic resonance imaging (MRI).⁶ However, BC can only be detected

when the BC mass can be measured in millimeters. At that time, the BC cells may have already metastasized, resulting in the patient missing their optimal treatment window.⁷ Detecting serum tumor markers from the blood test can also be used for BC diagnosing and recurrence monitoring, including cancer antigen (CA) 27.29, CA 15–3, CA 125, and carcinoembryonic antigen (CEA).^{8,9} However, patients with ulcerative colitis, pancreatitis, cirrhosis, or even healthy individuals can show positive results, which makes this BC diagnosis test unreliable.⁹

Benefiting from molecular probes, molecular imaging can visualize biological events at the cellular and molecular levels *in vivo*, thus having the potential to diagnose cancer at its early stage.^{10,11} Some preliminary studies have shown the preclinical diagnosis of cancer using molecular imaging.¹⁰ Among all the molecular imaging modalities, MRI is believed to be a promising approach because of its high spatial resolution, good soft tissue contrast, and non-ionizing radiation.¹² Moreover, with the progress of nanotechnology, superparamagnetic nanoparticles (NPs)—the key moiety of MR molecular probe with higher relaxivity—are emerging.¹³ As a result, the sensitivity and specificity of MR molecular imaging (MRMI) keeps improving, making it a more powerful and promising alternative for the early diagnosis of BC.¹⁴

The inefficiency of traditional therapy is another important factor contributing to the high fatality of BC. Upon diagnosis, the patient will undergo surgery, radiotherapy, or chemotherapy according to the BC stage.^{4,15} If the patient is estrogen receptor- (ER) or human epidermal growth factor receptor-2 (HER-2) positive, endocrine therapy (ET) or anti-HER-2 therapy will benefit the patient's recovery.¹⁶ However, surgery can only benefit if the BC has no metastasis. In addition, surgery can result in extensive trauma that can harm the immune balance and delay tumor healing.¹⁷ Because of their rapid proliferation, BC cells can be inhibited and killed by radiotherapy and chemotherapy. At the same time, other fast-growing cells that are essential for normal physiological homeostasis will be non-selectively killed and result in the side effects including emesis, alopecia, and emaciation.¹⁸ As a result, the dose of chemotherapy and radiotherapy is strictly limited in clinical practice, which may abate the killing effect and induce BC cell resistance to chemotherapy and radiotherapy.¹⁸ ET and anti-HER-2 therapy have recently been widely applied in the clinic and showed promising results.^{19,20} Nevertheless, about 15–20% of patients express none or few of these receptors, which greatly

compromises the therapeutic effect. In addition, some ER- or HER-2-positive cancer cells can become resistant to the treatment during the course of therapy.²⁰ Photothermal therapy (PTT) is an emerging and effective tumor treating strategy, having attracted great attention in recent years due to its noninvasive nature, controllability, and minimal side effects.²¹ Cells usually perform their physiological functions well at 37°C. As the temperature increases to 42–45°C, proteins aggregate and denature, resulting in the cell activity being significantly reduced. Further increasing the temperature to 48–60°C will cause cells to suffer irreversible damage and lead to apoptosis.²² Tumor cells are also more sensitive to high temperature than normal cells because of their rapid proliferation. Hyperthermia within cancer lesions can induce the release of CAs and proinflammatory cytokines to promote anticancer immunity, which kills cancer cells synergistically. It is known that photothermal agents (PTAs) are essential for PTT and the efficacy of PTT is closely related to the photothermal conversion efficiency (PCE). The higher the PCE of PTAs, the less the time and energy required for inducing cell death.²¹ Non-specific damage to surrounding tissues induced by the PTAs with higher PCE can be effectively minimized. Thus, PTAs with high PCE are desired for PTT.

Therefore, combining MRMI and PTT is expected to diagnose and treat BC early enough to improve its prognosis. The combination of MRMI and PTT can be theoretically achieved by injecting MRI and PTT agents simultaneously. Still, it is difficult to keep the two agents at the same pharmacokinetic and biodistribution profiles using the above strategy, leaving the combination of MRMI and PTT a challenge. Alternatively, using a Janus nanostructure composed of two functional moieties that can both shorten the relaxation time and convert light energy to thermal energy as the theranostic agents can, in practice, achieve the combination of MRMI and PTT. We previously synthesized a multifunctional Janus NP Fe₃O₄-Au_{shell} composed of two functional parts: Fe₃O₄ nanospheres that shorten the transverse relaxation time (*T*₂) and an Au_{shell} that serves as a PTA.²³ Fe₃O₄ NPs are the most widely studied and applied superparamagnetic NPs for MRMI. They show satisfactory relaxivity and good biocompatibility, with some iron oxide-based NPs (Resovis[®], Feridex I.V.[®]) approved for clinical use by the FDA.^{24,25} The Fe₃O₄ NPs are also easily modified by various ligands and biomacromolecules on the NP surface for multi-functionalization. Au_{shell} NPs are widely used

PTA for PTT and have shown good biocompatibility and high PCE. Benefitting from its hollow shell structure, the Au_{shell} has a high PCE and an absorption peak in the near-infrared (NIR) region, with minimal biological tissue absorption. This allows the laser energy to be more effectively absorbed and minimizes collateral damage to adjacent normal tissue.²⁶ Accordingly, Fe₃O₄-Au_{shell} Janus NPs may be considered an ideal candidate for the combination of MRMI and PTT.

Herein, we synthesized Fe₃O₄ NPs by thermolysis and Janus Fe₃O₄-Ag nanoparticles by reducing Ag⁺ on the surface of Fe₃O₄ nanoparticles followed by the seeded growth of Ag NPs. Based on the galvanic chemistry, Ag NPs were replaced with Au nanoshells, and Fe₃O₄-Au_{shell} Janus NPs were obtained. Fe₃O₄-Au_{shell} NPs were then characterized by transmission electron microscopy (TEM), high-resolution TEM (HRTEM), magnetic property measurement system (MPMS), microplate reader, electrophoretic light scattering (ELS), Fourier-transform infrared spectroscopy (FTIR), and inductively coupled plasma optical emission spectroscopy (ICP-OES). The cytotoxicity of Fe₃O₄-Au_{shell} NPs was measured using CCK-8 and hemolysis analysis. The relaxivity of Fe₃O₄-Au_{shell} coated by varied amounts of polyethylene glycol (PEG) was evaluated, and the in vitro PTT efficiency was determined. Finally, Fe₃O₄-Au_{shell}-PEG NPs were administered intratumorally for MR imaging and PTT in vivo to determine its feasibility for BC diagnosis and treatment.

Methods

Materials

Carbonyl iron (Fe(CO)₅) was obtained from the Xindingpengfei Technology Development Co., Ltd (Beijing, China). Chloroauric acid (HAuCl₄) and oleic acid (OA) were delivered by Sigma-Aldrich (USA). The 1-octadecene (ODE) was purchased from Acros (Shanghai, China). Tetramethyl ammonium hydroxide (TMAH), silver nitrate, and hydroxylamine hydrochloride were purchased from Adamas-beta (Shanghai, China). Trisodium citrate (TSC) was purchased from Sinopharm Chemical Reagent Co. Ltd (Beijing, China). H₂O₂ was purchased from Chuandong Chemical Co. Ltd (Chongqing, China). Thiol-PEG2K was bought from the Xi'an Ruixi Biological Technology Co., Ltd (Xi'an, China). The Cell Counting Kit-8 (CCK8), Calcein Acetoxymethyl (AM)/Propidium Iodide (PI) Cell Viability Assay Kit, and Penicillin-Streptomycin

Solution were purchased from Beyotime Biotechnology (Shanghai, China). Dulbecco's modified eagle medium (DMEM) and fetal bovine serum (FBS) were obtained from HyClone (Shanghai, China). Phosphate buffer saline (PBS) powder was purchased from Boster Biotechnology (Wuhan, China). All the chemicals were used as delivered and all glassware engaged in synthesis were rinsed by aqua regia and deionized water before use.

Nanoparticle Synthesis

Fe₃O₄-Ag_{seed}: The Fe₃O₄-Au_{shell} nanostructure was synthesized according to a previous method with some modifications that were initiated with the synthesis of Fe₃O₄-Ag_{seed}.²³ First, hydrophobic Fe₃O₄ nanoparticles were synthesized by thermolysis of Fe(CO)₅. Briefly, a mixture of 2.4 mL OA and 20 mL ODE was heated to 100°C with magnetic stirring and Ar gas bubbling. 0.5 h later, 0.4 mL of (3.04 mmol) Fe(CO)₅ was injected, and the system was heated to 295°C. After reacting for 1 h, the heating source was removed to cool down the dispersion to room temperature. The prepared NPs were washed with isopropanol three times and dispersed in 20 mL of hexane. To make the nanoparticles hydrophilic, the OA on the Fe₃O₄ surface was exchanged with TMAH. The synthesized Fe₃O₄ NPs were precipitated and dried to obtain a black-colored powder, followed by dispersed in 20 mL TMAH (10%) and sonicated until clear. The hydrophilic Fe₃O₄ NPs were then centrifuged and finally dispersed in 20 mL DI water. The Fe₃O₄-Ag_{seed} was further synthesized by reducing Ag⁺ on the surface of Fe₃O₄ NPs with the help of ferrous ion and citrate. A mixture of 40 mL DI water, 1 mL hydrophilic Fe₃O₄, and 1 mL 1% (w/v) TSC was heated to 60°C with magnetic stirring. Then, 500 µL of 0.17% (w/v) AgNO₃ was slowly added and reacted for 2 h. The dispersion was then irradiated under 254 nm ultraviolet light for 0.5 h at room temperature to ripen the Ag NPs. Afterwards, 4 mL of 1% TSC was added, and the system was reheated to 60°C, followed by the addition of 3.75 mL 0.17% AgNO₃ within 1 h. The solution was heated for another 0.5 h, and Fe₃O₄-Ag_{seed} was obtained.

Fe₃O₄-Au_{shell}: To make the absorption peak locate in the NIR region, the cavity to thickness ratio of Au_{shell} must be suitably fixed. Hence, we increased the Ag NPs' size by seeded-growth. A mixture of 5 mL Fe₃O₄-Ag_{seed}, 6.4 mL 1% (w/v) TSC, and 80 mL DI water was heated to 60°C under magnetic stirring. Then, 6.4 mL of 0.17% (w/v) AgNO₃ was added within 3 h followed by a reaction of

1 h to obtain $\text{Fe}_3\text{O}_4\text{-Ag}$ nanoparticles (Fe_3O_4 : 18 nm, Ag: 22 nm). Finally, $\text{Fe}_3\text{O}_4\text{-Au}_{\text{shell}}$ NPs were synthesized by coating an Au shell on the Ag core and then cavitating the Ag core based on the galvanic replacement chemistry.²⁷ Briefly, 5 mL of synthesized $\text{Fe}_3\text{O}_4\text{-Ag}$ NPs and 6.25 mM of hydroxylamine hydrochloride were mixed under magnetic stirring. Next, 5 mL of 0.465 mM HAuCl_4 was added within 12.5 min. When the color was stabilized, the dispersion was mixed with H_2O_2 (30%) in a volume ratio of 50:1 for 2 h to obtain $\text{Fe}_3\text{O}_4\text{-Au}_{\text{shell}}$. To improve the biocompatibility of the obtained $\text{Fe}_3\text{O}_4\text{-Au}_{\text{shell}}$, PEGs were conjugated on their surface by thiol-Au coordination. Equal volumes of Thiol-PEG2K and $\text{Fe}_3\text{O}_4\text{-Au}_{\text{shell}}$ were mixed at different molar ratios (PEG to $\text{Fe}_3\text{O}_4\text{-Au}_{\text{shell}}$: 0, 10, 40, 160, 640), followed by incubation at room temperature overnight. Then, unlinked PEG was removed by centrifugation. The obtained nanoparticles were termed as $\text{Fe}_3\text{O}_4\text{-Au}_{\text{shell}}\text{-PEG0}$, $\text{Fe}_3\text{O}_4\text{-Au}_{\text{shell}}\text{-PEG10}$, $\text{Fe}_3\text{O}_4\text{-Au}_{\text{shell}}\text{-PEG40}$, $\text{Fe}_3\text{O}_4\text{-Au}_{\text{shell}}\text{-PEG160}$, and $\text{Fe}_3\text{O}_4\text{-Au}_{\text{shell}}\text{-PEG640}$, accordingly.

Nanoparticle Characterization

The morphology and size distribution of NPs were analyzed using a TEM (HT7700, Hitachi, Japan). The element distribution was identified by EDS mapping (FEI Tecnai G2 F30, USA). Hysteresis loop was recorded by a MPMS3 (Quantum Design, USA). The Fe and Au content in nanoparticle were measured by an ICP-OES (Agilent ICPOES730, USA). The UV-Vis absorption spectrum of NPs was measured by a multi-mode microplate reader (Varioskan Flash, Thermo Scientific, USA). NPs' zeta potential was determined using ELS (Z3000, NICOMP, USA). We also verify the linking of PEG on the surface of $\text{Fe}_3\text{O}_4\text{-Au}_{\text{shell}}$ using FTIR (ALPHA II, BRUKER, USA).

Cells and Animals

Mouse breast cancer cells 4T1 were used for in vitro biocompatibility and photothermal efficiency analysis in the present study and purchased from Procell Co. Ltd (Wuhan, China). Cells were routinely cultured with complete medium, which was composed of 89% DMEM medium, 10% FBS, and 1% streptomycin and penicillin in a 5% CO_2 incubator at 37°C.

With permission from the Animal Welfare and Ethics Committee of the Army Medical University (No. 2019366), 10^6 4T1 cells were injected subcutaneously into the right thigh of nude mice to establish

a xenograft tumor model for in vivo MRI and PTT in this study. All the BALB/c nude mice (female, 5 weeks old) were purchased from HFK BIOSCIENCE Co. Ltd. (Beijing, China) and hosted in a specific pathogen free (SPF) environment at 20°C with a 12:12 dark/light cycle in the experimental animal center of Xinqiao Hospital, Army Medical University. All animal experiments were performed in accordance with the guidelines of Care and Use of Laboratory Animals of Ministry of Science and Technology of the People's Republic of China.

Cytotoxicity and Hemolysis

The cytotoxicity of $\text{Fe}_3\text{O}_4\text{-Au}_{\text{shell}}$ NPs was determined using a CCK-8 analysis. 4T1 cells were seeded into 96-well plates at 5000 cells per well and incubated with complete medium overnight to allow cell adhesion. Then, the complete medium in each well was replaced with media containing $\text{Fe}_3\text{O}_4\text{-Au}_{\text{shell}}$ of different concentrations (Fe: 0, 10, 20, 40, 80 ppm). After 24 h of incubation, the media containing $\text{Fe}_3\text{O}_4\text{-Au}_{\text{shell}}$ NPs were removed and the wells were washed three times with PBS. Afterwards, 100 μL of fresh complete medium and 10 μL of CCK8 working solution were added to each well, followed by 2 h of incubation. Finally, the absorbance of each well was measured with a multi-mode microplate reader (Varioskan Flash, Thermo Scientific, USA) at 450 nm.

For the hemolysis analysis, fresh red blood cells (RBCs) were harvested from a healthy BALB/c mouse and then washed 3 times and re-dispersed in 2 mL PBS for further use. About 0.2 mL RBCs-PBS dispersions were then added to 1 mL PBS (negative control), 1 mL DI water (positive control), 1 mL $\text{Fe}_3\text{O}_4\text{-Au}_{\text{shell}}$ dispersions in PBS with various Au concentrations (25, 50, 100 ppm). Then, all the samples were incubated in a 5% CO_2 incubator at 37°C for 2 h. After centrifuged, the supernatants were collected and measured at 545 nm with the multi-mode microplate reader to calculate the hemolysis rate.

MRI and PTT in vitro

The $\text{Fe}_3\text{O}_4\text{-Au}_{\text{shell}}\text{-PEG0}$, $\text{Fe}_3\text{O}_4\text{-Au}_{\text{shell}}\text{-PEG10}$, $\text{Fe}_3\text{O}_4\text{-Au}_{\text{shell}}\text{-PEG40}$, $\text{Fe}_3\text{O}_4\text{-Au}_{\text{shell}}\text{-PEG160}$, and $\text{Fe}_3\text{O}_4\text{-Au}_{\text{shell}}\text{-PEG640}$ dispersions with different concentrations (Fe: 0, 0.02, 0.04, 0.09, 0.18, 0.36 ppm) were MR-imaged in a Philips Ingenia 3 T MRI system with a head coil. The imaging parameters were as followed: turbo spin-echo (TSE) T_2 mapping: repetition time (TR) = 2000 ms, echo time (TE) = 13, 26, 39, 52, 65, and 78 ms; slice thickness/spacing = 2.5 mm/0.25 mm, field of view (FOV) =

164×164 mm². Linear regression of transverse relaxation rates ($1/T_2$) and Fe concentrations was conducted to obtain the slope as transverse relaxivity (r_2) values. The region of interest (ROI) was 40 mm² for both the signal intensity and relaxation time measurements.

To measure the heating performance, 0.5 mL of Fe₃O₄-Au_{shell}-PEG160 (Fe: 30 ppm, Au: 70 ppm) were irradiated under 808 nm laser at different power densities (0.65, 1.2, 2.0 W/cm²) for 5 min. Then, 0.5 mL of DI water, Fe₃O₄ (Fe: 30 ppm), Fe₃O₄-Au_{shell}-PEG160 (Fe: 10 ppm, Au: 23 ppm), and Fe₃O₄-Au_{shell}-PEG160 (Fe: 30 ppm, Au: 70 ppm) were irradiated under a 1.2 W/cm² laser for 5 min. A thermal camera (E8, FLIR, USA) was used to record the temperature every 30 s. We further evaluated the Fe₃O₄-Au_{shell}-PEG160 killing effect under PTT using CCK-8 assay and fluorescence staining. Cells (10⁴) were seeded into a 96-well plate overnight for adhesion. Afterwards, cells were classified into four groups and were treated differently as follows: group 1 and 3 cells were cultured with complete medium, while group 2 and 4 cells were incubated with complete medium containing Fe₃O₄-Au_{shell}-PEG160 (Fe: 30 ppm, Au: 70 ppm). Group 3 and group 4 cells were irradiated with a laser for 5 min at a power density of 0.65 W/cm², and groups 1 and 2 did not undergo any irradiation. At 24 h after treatment, the media containing Fe₃O₄-Au_{shell}-PEG160 NPs were removed, and the wells were washed three times with PBS. Afterwards, 100 µL of fresh complete medium and 10 µL of CCK8 working solution were added to each well, followed by 2 h of incubation. Finally, all the wells were measured at 450 nm under a microplate reader. Meanwhile, 100 µL of Calcein-AM/PI working solution was added to each well to stain all the cells with fluorescence for 30 min, and then all the cells were photographed under an inverted fluorescence microscope (IX83, Olympus, Japan).

MRI and PTT in vivo

At 7–8 days post-subcutaneous injection, the xenograft tumors were about 80 mm³ and used for MRI and PTT in vivo. The mice were anesthetized with isoflurane and maintained in a stereotaxic frame (R510IP, RWD Life Science, Shenzhen, China). Before and after Fe₃O₄-Au_{shell}-PEG160 (100 µL, Fe concentration: 40 ppm) administration intratumorally, the T_2 weighted images (T_2 WI) were acquired using a special mouse coil (MS40, Suzhou Medcoil Healthcare Co., Ltd) in a 3 T clinical GE MRI scanner according to the following parameters: TE= 70.5

ms, TR= 3040 ms, FOV = 60×60 mm², matrix = 288×192, slice thickness/spacing = 2.0 mm/0.2 mm, and number of excitation (NEX) = 6.

To determine the potential of Fe₃O₄-Au_{shell}-PEG160 for BC PTT in vivo, 12 tumor-bearing mice were equally divided into four groups and treated as follows: mice in group 1 received no additional treatment except for the routine feeding; mice in group 2 were injected with of 100 µL PBS intratumorally and then irradiated with 0.65 W/cm² 808 nm laser for 5 min; group 3 mice received intratumoral injections of 100 µL Fe₃O₄-Au_{shell}-PEG160 (Au: 70 ppm); and group 4 mice were injected with 100 µL of Fe₃O₄-Au_{shell}-PEG160 (Au: 70 ppm) intratumorally and then irradiated with a 0.65 W/cm² 808 nm laser for 5 min. For groups 2 and 4, the temperature of the mice's tumor was recorded every 0.5 min with a thermal imaging camera (E8, FLIR, USA) during laser irradiation. Tumor volume and body weight of all the mice were recorded every two days for 14 days. The tumor volume was calculated following the equation: length × width² × 0.5, in which the length and width are the largest longitudinal and transverse diameter. The relative tumor volume was defined as the ratio of current tumor volume compared with the same mouse's original volume and used for the comparison between different groups. At 14 days after treatment, all mice were humanely killed, and their main organs including the heart, lung, liver, left kidney, spleen were fixed with 4% formaldehyde for H&E staining.

Statistical Analysis

All values are expressed as the mean ± standard deviation (SD). Significant differences between different groups were assessed by a Student's unpaired *t*-test. The statistical significance is shown as: NS, not significant; **P* < 0.05; ***P* < 0.01; ****P* < 0.001.

Results and Discussion

Nanoparticle Synthesis and Characterization

The morphology and crystallinity of magnetic nanoparticles are closely related to their physical and chemical properties. Compared with coprecipitation and microemulsion, the NPs synthesized by thermal decomposition of carbonyl iron are usually of high uniformity and crystallinity, making the obtained NPs preferred for biomedical applications.^{28,29} The TEM image of the acquired Fe₃O₄ is shown in Figure 1A, indicating an average diameter of 18

± 2.1 nm and narrow size distribution. Benefitting from the reducibility of TSC and ferrous ions, silver nanoparticles could anchor on the surface of Fe_3O_4 to form a stable heterodimer structure (Figure 1B, Ag: 9.3 ± 1.8 nm). After seeded growth of Ag NPs, the Fe_3O_4 -Ag NPs with a typical Janus nano structure were successfully synthesized. By averaging 300 NPs using Nano Measurer, we were told that the Janus NPs had a uniform morphology with the size of 18 ± 2.2 nm (Fe_3O_4) and 22 ± 3.2 nm (Ag) (Figure 1D). According to galvanic replacement theory, Au^{3+} can be reduced and form an Au layer on Ag nanoparticle's surface by introducing the Au^{3+} ion to the Ag nanoparticle with the assistance of hydroxylamine hydrochloride.³⁰ Then, in the presence of H_2O_2 , the Ag core will be further oxidized to Ag^+ and drift away, leaving a hollow Au shell. As Figure 1E shows, the original Ag nanoparticle cores in the Janus structure were replaced by a hollow shell. The inner diameter of the hollow shell is about 20 ± 2.9 nm, which is about the same size as silver NPs, and the outer diameter was about 25 ± 3.3 nm, suggesting that the Fe_3O_4 - Au_{shell} is formed. It has been repetitively determined that Ag nanoparticles have a strong absorption cross section at about 400 nm, while Au nanosphere absorbs mostly at 520 nm.^{31,32} In addition, the hollowing of the Au nanosphere can significantly change its absorption profile. With the increase of the cavity-to-shell ratio, the absorption peak of the Au

nanostructures would be red-shifted and located within the NIR region when the ratio is 5:1.²⁶ This study showed consistent results (Figure 1C). Fe_3O_4 nanoparticles, which do not have a surface plasmon resonance (SPR) effect, exhibited a downward curve. After seeded growth, NPs showed a pointed peak at 412 nm, which was consistent with the Ag NPs' absorption, verifying the existence of Ag NPs. When the NPs were further galvanically replaced and etched, the 412 nm peak faded away and a gentle slope centered at 720 nm emerged, which represented the absorption pattern of Au shell and implicated the successful synthesis of Fe_3O_4 - Au_{shell} . To further identify the Janus NPs with nano Au shell visually, EDS mapping was performed. As Figure 1F shows, the nanoparticles were a typical Janus nanoparticle composed of two moieties. The solid spheres overlapped with the iron element and the hollow shells overlapped the Au element, confirming the results from TEM and absorption spectrum. We also determined the element concentration using ICP-OES, which showed that the synthesized Janus NPs contained both Fe and Au and their molar ratio was 1.5:1.

Cytotoxicity and Hemolysis

Good biocompatibility is a prerequisite of all inorganic nanoparticles for bio applications. Theoretically, iron is safe for organisms because of its essentiality for physiology homeostasis.³³ Au is an inert element, which will

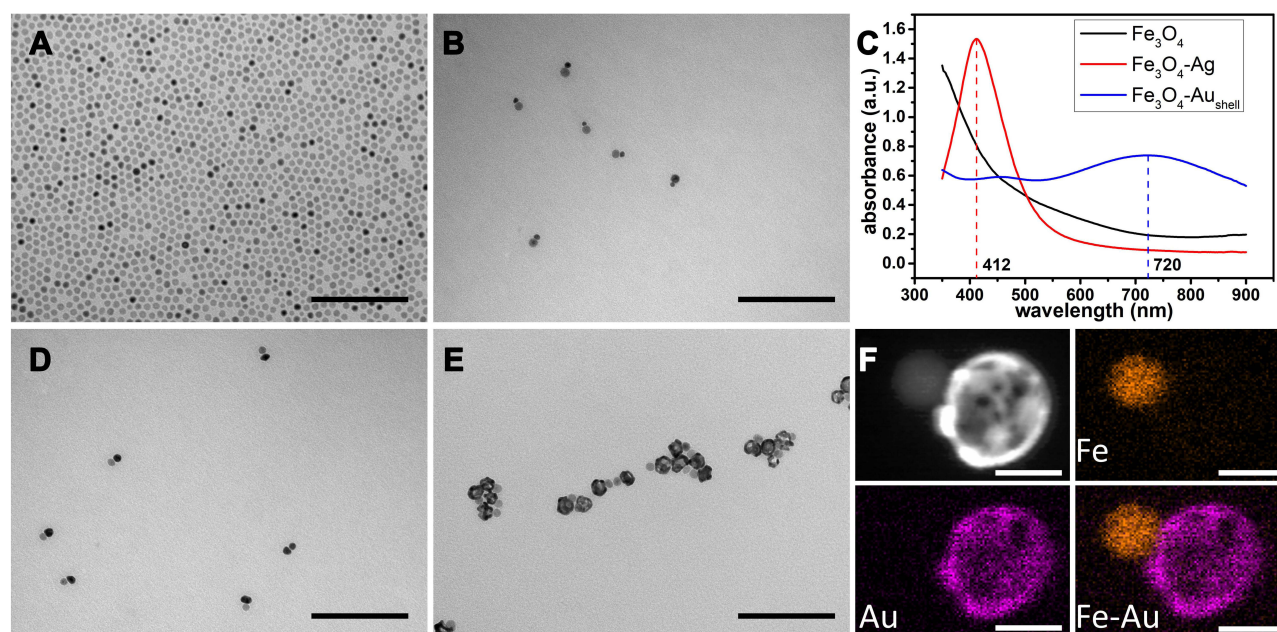


Figure 1 (A, B, D and E) TEM of Fe_3O_4 , Fe_3O_4 -Ag_{seeded}, Fe_3O_4 -Ag, Fe_3O_4 - Au_{shell} NPs, scale bar: 200 nm. (C) Absorbance of Fe_3O_4 , Fe_3O_4 -Ag, Fe_3O_4 - Au_{shell} NPs. (F) EDS mapping of Fe_3O_4 - Au_{shell} NP, scale bar: 20 nm.

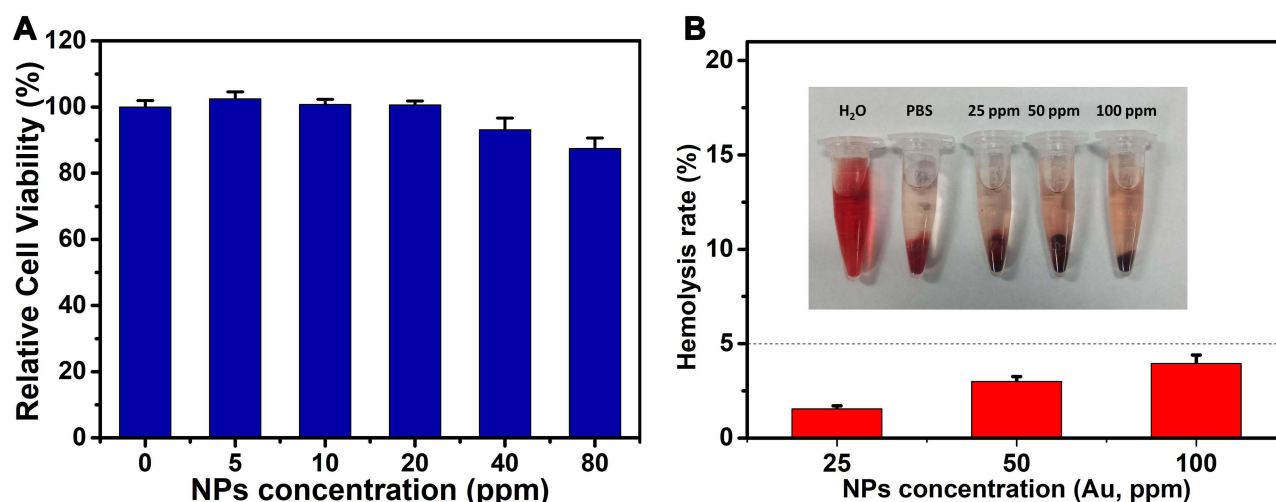


Figure 2 (A) Relative cell viability of 4T1 cells incubated with different concentrations of Fe₃O₄-Au_{shell} for 24 h. **(B)** Hemolysis rate of RBC incubated with Fe₃O₄-Au_{shell} dispersions in PBS of various concentrations.

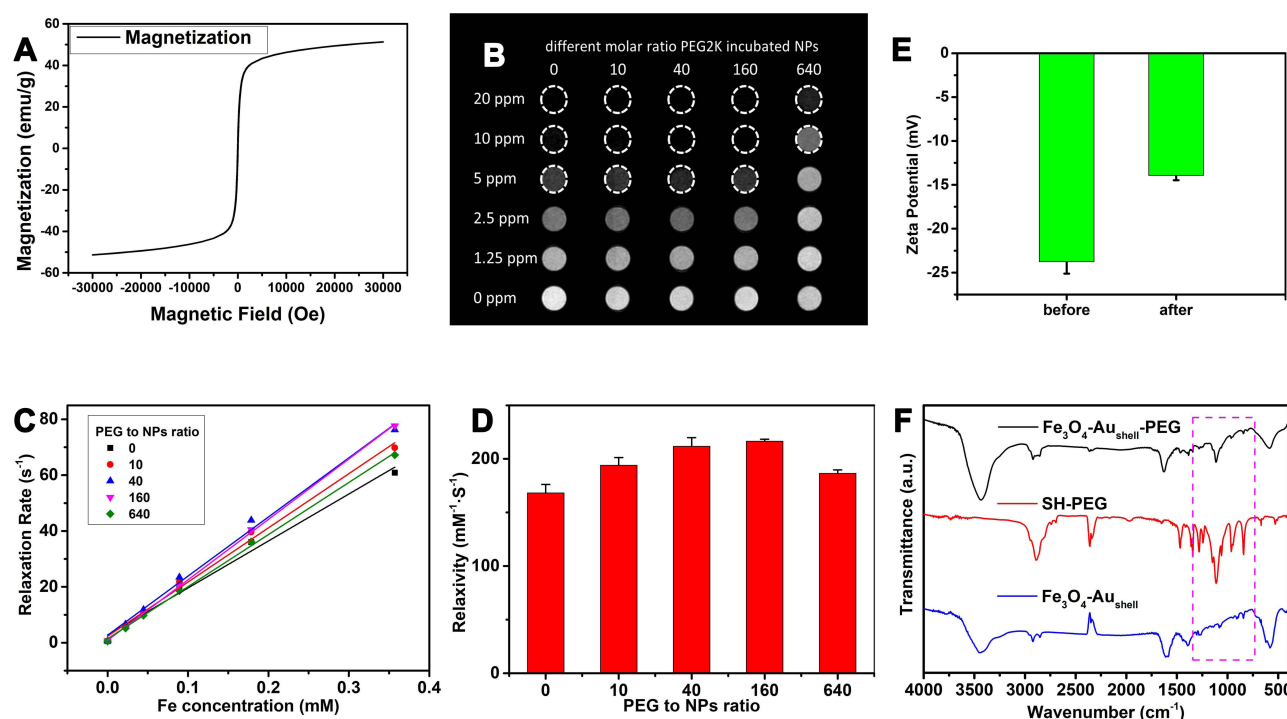
rarely react with other chemicals.³⁴ Hence, the synthesized Fe₃O₄-Au_{shell} NPs were considered to be of good biocompatibility. The results from the cytotoxicity assay confirmed our expectation as shown in Figure 2A. When the cells were co-incubated with Fe₃O₄-Au_{shell} NPs no higher than 20 ppm (5, 10, and 20 ppm), their viability was not different from the control cells. With the concentrations increasing, the viability decreased gradually. However, the cells still showed a high viability of 87% at 80 ppm, indicating good biosafety and paving the way for further bio application. The result of hemolysis analysis also confirmed the good biocompatibility of synthesized NPs (Figure 2B). As nanoparticles' concentration increased, hemolysis rate of RBCs rose from $1.6 \pm 0.15\%$ (25 ppm) to $3.0 \pm 0.26\%$ (50 ppm). However, even incubated with 100 ppm NPs, hemolysis rate of RBC was far below 5% ($3.9 \pm 0.45\%$) which was regarded as a safety requirement of NPs, demonstrating the biosafety and competency of Fe₃O₄-Au_{shell} NPs for further applications.³⁵

MRI and PTT in vitro

r_2 is believed to be the key to measuring the enhanced performance of the MRI contrast agents in T_2 WI.³⁶ According to the outer-sphere theory, the r_2 of superparamagnetic NPs is positively correlated with their saturation magnetization.³⁷ Therefore, we first recorded the hysteresis loop of the Fe₃O₄-Au_{shell} to evaluate their MRI enhancing performance. As shown in Figure 3A, the saturation magnetization of Fe₃O₄-Au_{shell} was 36 emu/g (mass measured from Fe₃O₄), which was consistent

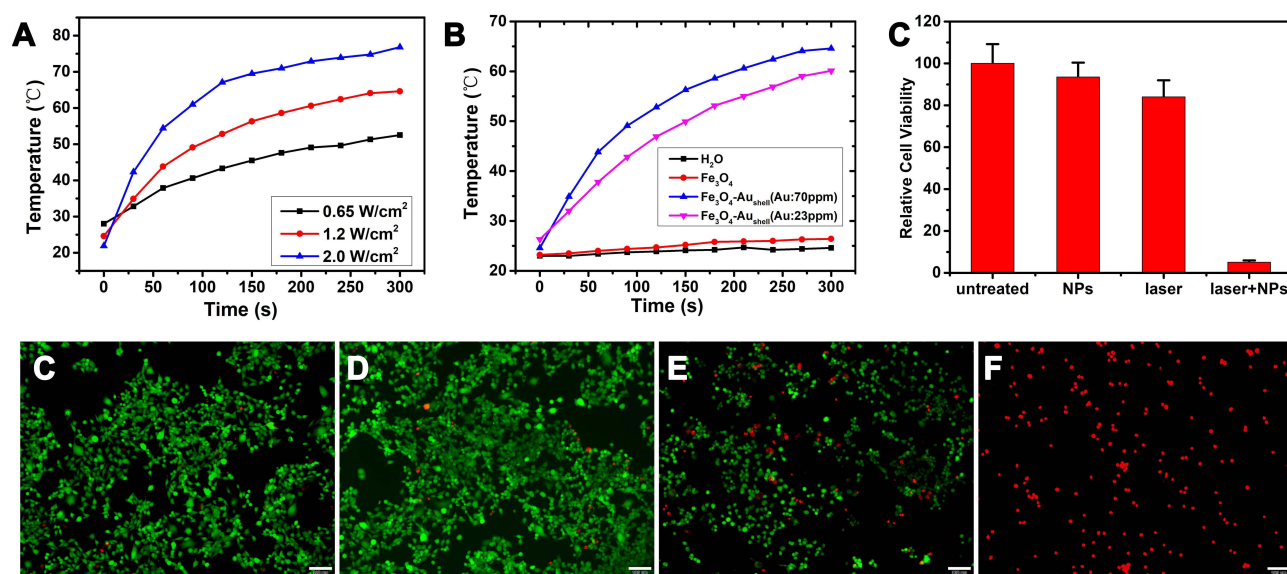
with the results from previous studies.³⁸ When the external magnetic field was absent, there was no residual magnetism, indicating their superparamagnetism, which is extremely essential to the in vivo bioapplications of magnetic NPs.

PEG is commonly used for improving inorganic nanoparticles' biocompatibility, retention time, and preventing NP aggregates.^{39–41} The NPs with more PEG usually show better biocompatibility and longer retention times.^{39,42,43} However, too much PEG on the nanoparticles will hinder the adjacent water accessibility, which may dampen its contrast efficiency. To obtain Fe₃O₄-Au_{shell} with enough r_2 and excellent biosafety simultaneously, we coated Fe₃O₄-Au_{shell} NPs with different amounts of PEG and studied them with MRI. To prove the successful modification of Fe₃O₄-Au_{shell} NPs with PEG, zeta potential analyses and FT-IR spectrum were applied. As Figure 3E showed, zeta potential of NPs changed from -23.75 ± 1.37 mV to -13.93 ± 0.55 mV after incubated with PEG. The zeta potential change could be contributed from the partly replacement of negatively charged citrate ligand on the surface of Fe₃O₄-Au_{shell} Janus NPs by PEG which was of electroneutrality, indirectly proving the successful modification of Fe₃O₄-Au_{shell} nanoparticles by PEG.⁴⁴ FTIR showed an intense peak at 1113 cm^{-1} after PEG incubation, which matches the characteristic C-O stretching vibration and confirms the successful linking of PEG on the NPs decisively (Figure 3F). The T_2 WI images of NPs were illustrated as Figure 3B. Due to NPs' shortening T_2 ability, the images



became darker as the concentration increased. However, $\text{Fe}_3\text{O}_4\text{-Au}_{\text{shell}}\text{-PEG10}$, $\text{Fe}_3\text{O}_4\text{-Au}_{\text{shell}}\text{-PEG40}$, $\text{Fe}_3\text{O}_4\text{-Au}_{\text{shell}}\text{-PEG160}$ manifested a darker appearance

compared with $\text{Fe}_3\text{O}_4\text{-Au}_{\text{shell}}\text{-PEG0}$, $\text{Fe}_3\text{O}_4\text{-Au}_{\text{shell}}\text{-PEG640}$ at the same concentration. To study this observation quantitatively, the T_2 from each sample was used to



calculate r_2 through linear regression. As Figure 3C and D shows, when the PEG amount increased, r_2 of MNPs gradually increased from $170 \text{ mM}^{-1}\text{s}^{-1}$ to $216 \text{ mM}^{-1}\text{s}^{-1}$. When the incubation ratio reached 640 ($\text{Fe}_3\text{O}_4\text{-Au}_{\text{shell}}\text{-PEG640}$), r_2 decreased to $190 \text{ mM}^{-1}\text{s}^{-1}$. This phenomenon may result from that PEG can improve the accessibility of surrounding water molecules to Fe_3O_4 NPs and result in a notable elevation of r_2 . However, too many PEGs attaching to $\text{Fe}_3\text{O}_4\text{-Au}_{\text{shell}}$ surface will not only impede water accessibility but also increase the NPs' size, leading to a decrease in the r_2 of $\text{Fe}_3\text{O}_4\text{-Au}_{\text{shell}}$ NPs. These results suggested that $\text{Fe}_3\text{O}_4\text{-Au}_{\text{shell}}\text{-PEG160}$ was optimal for MR T_2 imaging and was consequently used in the following experiment.

The killing effect of PTT is mainly derived from the elevated temperature induced by laser irradiation.⁴⁵ Therefore, the photothermal efficiency of a certain PTA under various experimental conditions is essential for optimizing the PTT strategy. As shown in Figure 4A, after 5 min of exposure, different powered lasers led to different temperature rises of $\text{Fe}_3\text{O}_4\text{-Au}_{\text{shell}}\text{-PEG160}$ at

a fixed concentration (Fe: 30 ppm, Au: 70 ppm). The dispersion reached 75°C with a ΔT of nearly 50°C at 2.0 W/cm^2 , while the dispersion showed much lower temperatures of 64.6°C and 52.5°C after 1.2 W/cm^2 and 0.65 W/cm^2 laser irradiation. When the laser power was fixed at 1.2 W/cm^2 , the $\text{Fe}_3\text{O}_4\text{-Au}_{\text{shell}}\text{-PEG160}$ dispersions showed different temperatures as shown in Figure 4B. NPs with higher concentration (Fe: 30 ppm, Au: 70 ppm) heated the water more efficiently than the lower ones (Fe: 10 ppm, Au: 23 ppm) (64.6°C VS 60.1°C). By contrast, the DI water containing Fe_3O_4 NPs and no NPs were not heated and showed no temperature rise. Because cells can be efficiently killed at 50°C ,⁴⁶ the concentration of $\text{Fe}_3\text{O}_4\text{-Au}_{\text{shell}}\text{-PEG160}$ was fixed at 100 ppm (Fe + Au), and the laser power was fixed at 0.65 W/cm^2 for the following study to minimize non-specific damage to PTT. Subsequently, in vitro PTT was performed to verify this assumption. After 5 min of irradiation and overnight incubation, all the cells were analyzed by CCK-8 assay for viability evaluation and stained with Calcein-AM/PI for fluorescence imaging.

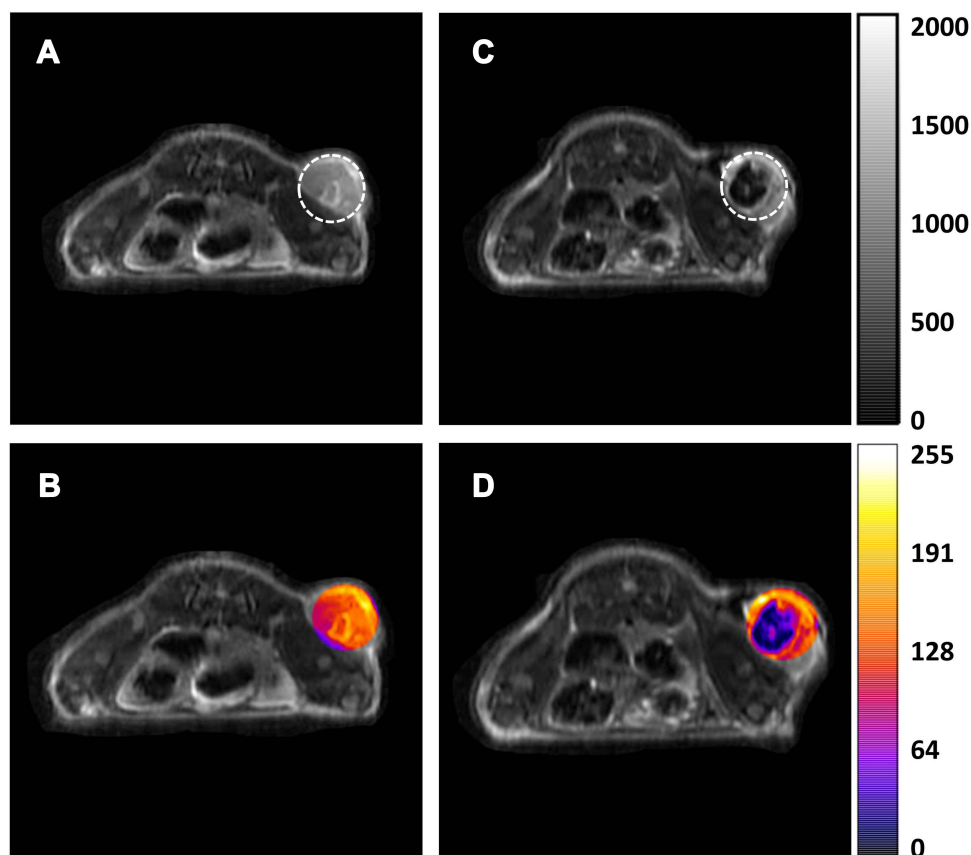


Figure 5 T_2 WI images of tumor before (A) and after (C) $\text{Fe}_3\text{O}_4\text{-Au}_{\text{shell}}$ injection, signal intensity rapidly decreased from 1487 ± 249 to 586 ± 233 . Pseudo color was added by ImageJ (B and D).

As Figure 4C shows, $\text{Fe}_3\text{O}_4\text{-Au}_{\text{shell}}\text{-PEG160}$ NPs had ignorable influence in cell viability ($93.5 \pm 6.9\%$). The viability of cells from laser+PBS group was slightly lowered ($84 \pm 8.0\%$) due to the minor temperature rising after laser irradiation. In contrast, only few cells ($5.1 \pm 0.8\%$) were alive after treatment in the NPs+laser group, which indicated a drastic PTT effect of $\text{Fe}_3\text{O}_4\text{-Au}_{\text{shell}}\text{-PEG160}$. Fluorescence microscope imaging showed a consistent result. Dead cells were hardly seen in the untreated group (Figure 4D), while some sporadic red dots were observed in the $\text{Fe}_3\text{O}_4\text{-Au}_{\text{shell}}\text{-PEG160}$ group (Figure 4E) and laser group (Figure 4F). In contrast, the dead cells were present in every view of the $\text{Fe}_3\text{O}_4\text{-Au}_{\text{shell}}\text{-PEG160}$ +laser group (Figure 4G), demonstrating the good PTT effect of $\text{Fe}_3\text{O}_4\text{-Au}_{\text{shell}}\text{-PEG160}$ in vitro.

MRI and PTT in vivo

To further determine the potential of $\text{Fe}_3\text{O}_4\text{-Au}_{\text{shell}}\text{-PEG}$ as MRI CAs, $\text{Fe}_3\text{O}_4\text{-Au}_{\text{shell}}\text{-PEG160}$ NPs were administered intratumorally and then imaged in a 3 T MRI scanner. As shown in Figure 5A and B, xenograft tumors exhibited a signal intensity of 1487 ± 249 in T_2 WI before NPs injection. After intratumoral injection (Figure 5C and D), the signal intensity rapidly decreased to 586 ± 233 . This significant signal intensity drop of 60.6% in T_2 WI suggested that $\text{Fe}_3\text{O}_4\text{-Au}_{\text{shell}}\text{-PEG160}$ NPs are qualified to serve as MRI T_2 contrast agent.

Preferred PTT requires that the cancer cells be effectively killed and adjacent normal tissue damage was avoided. Accordingly, the tumor should be irradiated under the laser with a lower power in a shorter time period

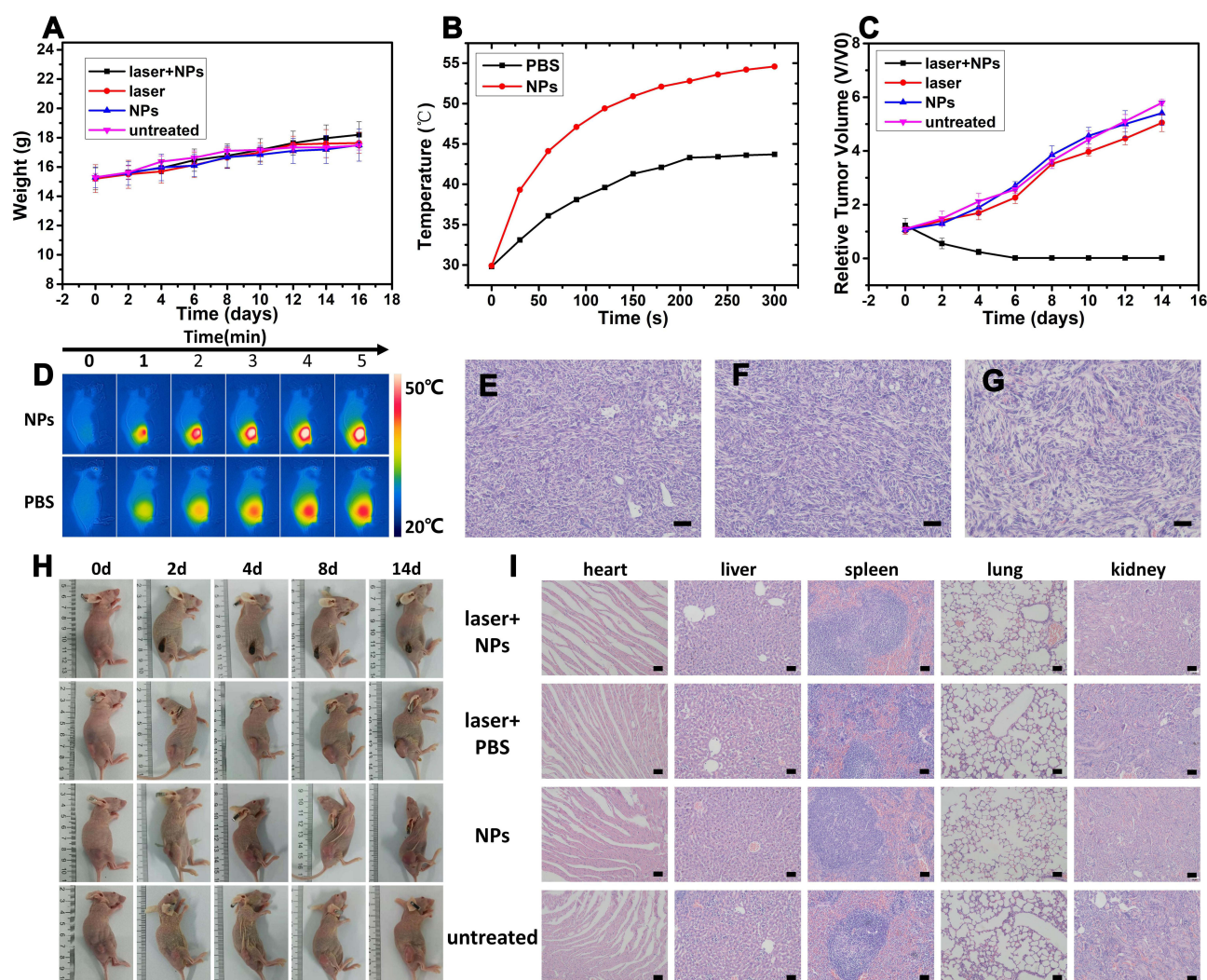


Figure 6 (A) Mice weight, (C) mice tumor volume and (H) tumor photograph at different time points after treatment. Mice tumor's thermal images (D) and temperature change (B) under 0.65 W/cm^2 laser irradiation for 5 min. (E–G) H&E staining of tumor from laser, NPs and untreated groups (scale bar: $50 \mu\text{m}$). (I) H&E staining of vital organs harvested from different group mice at 14th day after treatment (scale bar: $50 \mu\text{m}$).

with the help of PTAs with superb PCE.^{21,22} Herein, all the tumors were irradiated under 0.65 W/cm² laser for 5 min. The tumor temperature of the PBS+laser group rose to only 43.7°C, which is far below the killing threshold (50°C). In contrast, the tumor temperature of the Fe₃O₄-Au_{shell}-PEG+laser group rose rapidly, reaching 50°C at 2.5 min and finally reaching 54.6°C at 5 min (Figure 6B and D). After treatment, tumors of Fe₃O₄-Au_{shell}-PEG+laser group shrink rapidly, and the relative volume dropped from 1.0 at the beginning to 0.55 in the 2nd day to 0.24 in the 3rd day (Figure 6C). Six days after treatment, there was no visible tumor except a black scar. The tumors in the other groups (untreated, laser+PBS, Fe₃O₄-Au_{shell}-PEG) grew fast. The relative volume of these tumors (untreated, laser+PBS, Fe₃O₄-Au_{shell}-PEG) reached 3.63, 3.82, 3.85 in the 8th day and rose to 5.79, 5.05, 5.41 in the 14th day. In the H&E photos, cells of the laser, NPs, and untreated groups all showed regular morphology. There were no obvious necrotic or inflammatory cells that could be seen in any view of the section (Figure 6E–G). The biosafety of Fe₃O₄-Au_{shell}-PEG160 was also evaluated. As shown in Figure 6A and H, the mice neither lost weight nor showed abnormal behavior. As expected, organs from mice treated with Fe₃O₄-Au_{shell}-PEG showed no observable inflammation or other changes (Figure 6I). Based on these promising results, it is reasonable to conclude that Fe₃O₄-Au_{shell}-PEG NPs are an effective PTA for BC PTT in vivo.

Conclusion

In conclusion, to address the diagnosis and therapeutic straits in BC, we successfully synthesized Fe₃O₄-Au_{shell} NPs which had uniform Janus-like morphology and explored its theranostic potential. After synthesis and characterization, Fe₃O₄-Au_{shell} showed a favorable biocompatibility from the cell viability and hemolysis test, which is prerequisite for bioapplications. PEG linking did not harm the nanoparticle's MRI performance. In the contrast, enhanced r_2 could be achieved by a suitable incubation ratio. In vitro measurements verified the r_2 and PTT efficacy of Fe₃O₄-Au_{shell}-PEG, which fulfills the demand for simultaneously effective MR imaging and PTT treatment. Based on this promising result, Fe₃O₄-Au_{shell}-PEG NPs were injected in 4T1 xenograft models and then were MR imaged and irradiated under 808 nm laser. Obvious T₂ enhancement and tumor killing effect were observed, while no noticeable side effect was seen until the end of experiment. Given

the exciting outcomes, Fe₃O₄-Au_{shell}-PEG manifested its competences in MR imaging and PTT treatment, and thus provides a promising alternative for future BC theranostics.

Acknowledgments

The research was supported by the Research Project of Army Medical University (2018XY12), Miaopu Foundation of Army Medical University (No. 2019R059), Natural Science Foundation of Chongqing (No. cstc2018jcyjAX0321, cstc2017jcyjBX0038 and cstc2020jcyj-msxmX1017) and Basic Research Project of Army Medical University (2021-2018-070).

Disclosure

The authors report no conflicts of interest in this work.

References

- Veronesi U, Boyle P, Goldhirsch A, Orecchia R, Viale G. Breast cancer. *Lancet*. 2005;365(9472):1727–1741. doi:10.1016/S0140-6736(05)66546-4
- Sung H, Ferlay J, Siegel RL, et al. Global cancer statistics 2020: GLOBOCAN estimates of incidence and mortality worldwide for 36 cancers in 185 countries. *CA Cancer J Clin*. 2021;71(3):209–249.
- DeSantis CE, Ma J, Gaudet MM, et al. Breast cancer statistics, 2019. *CA Cancer J Clin*. 2019;69(6):438–451.
- Cardoso F, Kyriakides S, Ohno S, et al. Early breast cancer: ESMO clinical practice guidelines for diagnosis, treatment and follow-up. *Ann Oncol*. 2019;30(8):1194–1220. doi:10.1093/annonc/mdz173
- McDonald ES, Clark AS, Tchou J, Zhang P, Freedman GM. Clinical diagnosis and management of breast cancer. *J Nucl Med*. 2016;57 (Supplement1):9S–16S. doi:10.2967/jnumed.115.157834
- Myers ER, Moorman P, Gierisch JM, et al. Benefits and harms of breast cancer screening: a systematic review. *JAMA*. 2015;314 (15):1615–1634. doi:10.1001/jama.2015.13183
- Smith RA, Andrews KS, Brooks D, et al. Cancer screening in the United States, 2018: a review of current American cancer society guidelines and current issues in cancer screening. *CA Cancer J Clin*. 2018;68(4):297–316.
- Wang W, Xu X, Tian B, et al. The diagnostic value of serum tumor markers CEA, CA19-9, CA125, CA15-3, and TPS in metastatic breast cancer. *Clin Chim Acta*. 2017;470:51–55. doi:10.1016/j.cca.2017.04.023
- Jafari SH, Saadatpour Z, Salmaninejad A, et al. Breast cancer diagnosis: imaging techniques and biochemical markers. *J Cell Physiol*. 2018;233(7):5200–5213. doi:10.1002/jcp.26379
- Miller JC, Thrall JH. Clinical molecular imaging. *J Am Coll Radiol*. 2004;1(1 Suppl):4–23. doi:10.1016/S1546-1440(03)00025-5
- Padmanabhan P, Kumar A, Kumar S, Chaudhary RK, Gulyás B. Nanoparticles in practice for molecular-imaging applications: an overview. *Acta Biomater*. 2016;41:1–16. doi:10.1016/j.actbio.2016.06.003
- Logothetis NK. What we can do and what we cannot do with fMRI. *Nature*. 2008;453(7197):869–878. doi:10.1038/nature06976
- Jun YW, Jang JT, Cheon J. Magnetic nanoparticle assisted molecular MR imaging. *Adv Exp Med Biol*. 2007;620:85–106.
- Shakil MS, Hasan MA, Sarker SR. Iron oxide nanoparticles for breast cancer theranostics. *Curr Drug Metab*. 2019;20(6):446–456. doi:10.2174/1389200220666181122105043

15. Fiorica JV. Breast cancer screening, mammography, and other modalities. *Clin Obstet Gynecol*. 2016;59(4):688–709. doi:10.1097/GRF.0000000000000246
16. Adolphi NL, Butler KS, Lovato DM, et al. Imaging of Her2-targeted magnetic nanoparticles for breast cancer detection: comparison of SQUID-detected magnetic relaxometry and MRI. *Contrast Media Mol Imaging*. 2012;7(3):308–319. doi:10.1002/cmmi.499
17. Tyagi NK, Dhesy-Thind S. Clinical practice guidelines in breast cancer. *Curr Oncol*. 2018;25(Suppl 1):S151–s160. doi:10.3747/co.25.3729
18. Castaneda SA, Strasser J. Updates in the treatment of breast cancer with radiotherapy. *Surg Oncol Clin N Am*. 2017;26(3):371–382. doi:10.1016/j.soc.2017.01.013
19. Reinbolt RE, Mangini N, Hill JL, et al. Endocrine therapy in breast cancer: the neoadjuvant, adjuvant, and metastatic approach. *Semin Oncol Nurs*. 2015;31(2):146–155. doi:10.1016/j.soncn.2015.02.002
20. Yao M, Fu P. Advances in anti-HER2 therapy in metastatic breast cancer. *Chin Clin Oncol*. 2018;7(3):27. doi:10.21037/cco.2018.05.04
21. Liu Y, Bhattarai P, Dai Z, Chen X. Photothermal therapy and photoacoustic imaging via nanotheranostics in fighting cancer. *Chem Soc Rev*. 2019;48(7):2053–2108.
22. Zhou Z, Yan Y, Hu K, et al. Autophagy inhibition enabled efficient photothermal therapy at a mild temperature. *Biomaterials*. 2017;141:116–124. doi:10.1016/j.biomaterials.2017.06.030
23. Zeng J, Gong M, Wang D, et al. Direct synthesis of water-dispersible magnetic/plasmonic heteronanostructures for multimodality biomedical imaging. *Nano Lett*. 2019;19(5):3011–3018. doi:10.1021/acs.nanolett.9b00171
24. Reimer P, Balzer T. Ferucarbotran (Resovist): a new clinically approved RES-specific contrast agent for contrast-enhanced MRI of the liver: properties, clinical development, and applications. *Eur Radiol*. 2003;13(6):1266–1276. doi:10.1007/s00330-002-1721-7
25. Ferumoxides. Drugs and Lactation Database (LactMed). US: National Library of Medicine; 2006.
26. Xia X, Wang Y, Ruditskiy A, Xia Y. 25th anniversary article: galvanic replacement: a simple and versatile route to hollow nanostructures with tunable and well-controlled properties. *Adv Mater*. 2013;25(44):6313–6333. doi:10.1002/adma.201302820
27. He D, Garg S, Waite TD. H₂O₂-mediated oxidation of zero-valent silver and resultant interactions among silver nanoparticles, silver ions, and reactive oxygen species. *Langmuir*. 2012;28(27):10266–10275. doi:10.1021/la300929g
28. Laurent S, Forge D, Port M, et al. Magnetic iron oxide nanoparticles: synthesis, stabilization, vectorization, physicochemical characterizations, and biological applications. *Chem Rev*. 2008;108(6):2064–2110.
29. Yu WW, Falkner JC, Yavuz CT, Colvin VL. Synthesis of monodisperse iron oxide nanocrystals by thermal decomposition of iron carboxylate salts. *Chem Commun*. 2004;(20):2306–2307. doi:10.1039/b409601k
30. Shahjamali MM, Bosman M, Cao S, et al. Gold coating of silver nanoprisms. *Adv Funct Mater*. 2012;22(4):849–854. doi:10.1002/adfm.201102028
31. Verma A, Mehata MS. Controllable synthesis of silver nanoparticles using Neem leaves and their antimicrobial activity. *J Rad Res Appl Sci*. 2016;9(1):109–115. doi:10.1016/j.jrras.2015.11.001
32. Jain PK, Lee KS, El-Sayed IH, El-Sayed MA. Calculated absorption and scattering properties of gold nanoparticles of different size, shape, and composition: applications in biological imaging and biomedicine. *J Phys Chem B*. 2006;110(14):7238–7248. doi:10.1021/jp057170o
33. Zimmermann MB, Hurrell RF. Nutritional iron deficiency. *Lancet*. 2007;370(9586):511–520. doi:10.1016/S0140-6736(07)61235-5
34. Singh P, Pandit S, Mokkapati V, Garg A, Ravikumar V, Mijakovic I. Gold nanoparticles in diagnostics and therapeutics for human cancer. *Int J Mol Sci*. 2018;19(7):1979. doi:10.3390/ijms19071979
35. Yin T, Li Y, Ren Y, et al. Phagocytosis of polymeric nanoparticles aided activation of macrophages to increase atherosclerotic plaques in ApoE^{−/−} mice. *J Nanobiotechnology*. 2021;19(1):121. doi:10.1186/s12951-021-00863-y
36. Lee H, Shin T-H, Cheon J, Weissleder R. Recent developments in magnetic diagnostic systems. *Chem Rev*. 2015;115(19):10690–10724. doi:10.1021/cr500698d
37. Zhao Z, Zhou Z, Bao J, et al. Octapod iron oxide nanoparticles as high-performance T2 contrast agents for magnetic resonance imaging. *Nat Commun*. 2013;4(1):2266. doi:10.1038/ncomms3266
38. Dorniani D, Hussein MZB, Kura AU, Fakurazi S, Shaari AH, Ahmad Z. Sustained release of prindopril erbumine from its chitosan-coated magnetic nanoparticles for biomedical applications. *Int J Mol Sci*. 2013;14(12):23639–23653. doi:10.3390/ijms141223639
39. Niidome T, Yamagata M, Okamoto Y, et al. PEG-modified gold nanorods with a stealth character for in vivo applications. *J Control Release*. 2006;114(3):343–347.
40. Blanco E, Shen H, Ferrari M. Principles of nanoparticle design for overcoming biological barriers to drug delivery. *Nat Biotechnol*. 2015;33(9):941–951. doi:10.1038/nbt.3330
41. Manson J, Kumar D, Meenan BJ, Dixon D. Polyethylene glycol functionalized gold nanoparticles: the influence of capping density on stability in various media. *Gold Bull*. 2011;44(2):99–105. doi:10.1007/s13404-011-0015-8
42. Fleischer CC, Payne CK. Nanoparticle-cell interactions: molecular structure of the protein corona and cellular outcomes. *Acc Chem Res*. 2014;47(8):2651–2659. doi:10.1021/ar500190q
43. Zhang W. Nanoparticle aggregation: principles and modeling. *Adv Exp Med Biol*. 2014;811:19–43.
44. Qian W, Murakami M, Ichikawa Y, Che Y. Highly efficient and controllable PEGylation of gold nanoparticles prepared by femtosecond laser ablation in water. *J Phys Chem C*. 2011;115(47):23293–23298. doi:10.1021/jp2079567
45. Xu W, Lin Q, Yin Y, et al. A review on cancer therapy based on the photothermal effect of gold nanorod. *Curr Pharm Des*. 2019;25(46):4836–4847. doi:10.2174/1381612825666191216150052
46. Ding F, Gao X, Huang X, et al. Polydopamine-coated nucleic acid nanogel for siRNA-mediated low-temperature photothermal therapy. *Biomaterials*. 2020;245:119976. doi:10.1016/j.biomaterials.2020.119976

International Journal of Nanomedicine

Publish your work in this journal

The International Journal of Nanomedicine is an international, peer-reviewed journal focusing on the application of nanotechnology in diagnostics, therapeutics, and drug delivery systems throughout the biomedical field. This journal is indexed on PubMed Central, MedLine, CAS, SciSearch®, Current Contents®/Clinical Medicine,

Journal Citation Reports/Science Edition, EMBASE, Scopus and the Elsevier Bibliographic databases. The manuscript management system is completely online and includes a very quick and fair peer-review system, which is all easy to use. Visit <http://www.dovepress.com/testimonials.php> to read real quotes from published authors.

Submit your manuscript here: <https://www.dovepress.com/international-journal-of-nanomedicine-journal>